Journal of Catalysis **182,** 378–389 (1999)
Article ID jcat.1998.2335, available online at http://www.idealibrary.com on IDEAL®

Redox Property–Local Structure Relationships in the Rh-Loaded CeO_2–ZrO_2 Mixed Oxides

Gilberto Vlaic, Roberta Di Monte, Paolo Fornasiero, Emiliano Fonda, Jan Kašpar,[1] and Mauro Graziani

Dipartimento di Scienze Chimiche, Università di Trieste, 34127 Trieste, Italy

Received July 13, 1998; revised October 26, 1998; accepted November 3, 1998

The local structure of the M–O bond in CeO_2–ZrO_2 mixed oxides is investigated with the aim of finding a correlation between structural parameters and oxygen exchange properties. It is found that insertion of ZrO_2 into the CeO_2 lattice strongly perturbs the symmetry of the M–O bond. As the content of CeO_2 in CeO_2–ZrO_2 solid solution is increased from 20 to 80 mol%, tetragonal, (t, t', t'') and cubic phases are formed. The local symmetry of the Zr–O bond is strongly perturbed by the increase in CeO_2 content while no significant modification of the first Ce–O coordination sphere is found, except for lengthening of the Ce–O bond consistent with lattice parameter increase. The perturbation of the Zr–O coordination sphere, which leads to highly disordered oxygen in the lattice, is indicated as responsible for the high oxygen mobility in CeO_2–ZrO_2 mixed oxides. © 1999 Academic Press

Key Words: **CeO_2–ZrO_2 mixed oxides; Rh/CeO_2–ZrO_2 mixed oxides; redox properties; CeO_2–ZrO_2 solid solution; local structure; oxygen storage capacity; three-way catalysts; Raman and EXAFS characterization.**

1. INTRODUCTION

Pollution problems are an important area of scientific research. In particular, three-way catalysts (TWCs), which are used to simultaneously abate NO_x, CO, and hydrocarbons (HC) contained in automotive exhaust, have been extensively studied due to the increasingly tight legislation requirements for pollution abatement (1). Since 1995, the fourth generation of automotive catalysts has been employed (2); these are based mainly on precious metals (PMs, mostly Pd) supported on stabilized Al_2O_3 and a thermally stable oxygen storage/release promoter which acts as an oxygen buffer in the exhaust. The capacity to store and release oxygen [oxygen storage capacity (OSC)] allows one to enlarge the operating air-to-fuel (A/F) window, by keeping the oxidant/reductant ratio close to stoichiometric level where the highest conversions are attained (3). Traditionally, high-surface-area CeO_2 has been employed for this purpose (3). A major drawback of CeO_2 is the loss of OSC on sintering, leading to deactivation of the catalyst (4). Insertion of ZrO_2 into the CeO_2 lattice, leading to formation of a CeO_2–ZrO_2 solid solution, has been shown to dramatically increase both thermal stability and OSC (5, 6).

We have investigated OSC in detail and proposed that the ability of ZrO_2 to promote reduction of CeO_2 in the bulk should be related to the structural modifications of the fluorite lattice of CeO_2 induced by insertion of ZrO_2 (7, 8). In a previous paper the correlation between the reduction behavior of a $Ce_{0.5}Zr_{0.5}O_2$ mixed oxide and its structural properties was reported (8). Here we extend our investigation to the whole range of compositions by varying x in $Ce_xZr_{1-x}O_2$ mixed oxides.

2. EXPERIMENTAL

2.1. Data Collection and Sample Preparation

All the catalysts were from previous studies (6, 7, 9). They were prepared by solid-state synthesis, by firing mixtures of the oxides at 1873 K for 1 h. $RhCl_3$ was employed as metal precursor. Rh nominal loading was 0.5 wt%.

EXAFS spectra of the Zr K edge of standard and catalytic samples were collected at LURE on beamline EXAFS I using a Si(331) channel-cut monochromator. Detectors were two ionization chambers filled with Ar at atmospheric pressure. All samples were crushed in a mortar to obtain a fine powder and then pressed at 7.6×10^8 N m^{-2} to obtain self-supporting pellets. Weights of samples were calculated to obtain a total absorption coefficient of 2.5. Zirconium K-edge spectra had been collected at room temperature (RT) in the energy interval 17.9–18.9 keV with 2-eV step and 2-s integration time.

EXAFS spectra of the Ce L_{III} edge of standard (CeO_2) and catalytic samples were collected on the same beamline as Zr K-edge spectra. The ionization chambers were filled with air at atmospheric pressure. The data were recorded at RT with a 2-eV step from 5680 to 6190 eV and 2-s integration time. The samples were prepared by mixing powders with boron nitride in a mortar and then pressed at 7.6×10^8 N m^{-2}. Weights of samples were calculated to obtain a total absorption coefficient of 2.5.

---

[1] To whom correspondence should be addressed. E-mail: kaspar@univ.trieste.it. Fax: +39–040–6763903.

0021-9517/99 $30.00

Powder XRD spectra were collected on a Siemens Kristalloflex Model F Instrument (Ni-filtered Cu$K\alpha$). Cell parameters were determined from the XRD patterns using the TREOR90 program. FT-Raman spectra were measured on a Perkin–Elmer 2000 FT-Raman spectrometer with diode-pumped YAG laser and a RT super InGaAs detector. The laser power was 50–400 mW.

2.2. EXAFS Analysis Procedure

Analysis of Zr K-edge EXAFS spectra was performed by Fourier filtering method using EXAFS pour le Mac software (10). The EXAFS signal was isolated from the total absorption using the following procedure. The threshold was chosen at half-height of edge jump, then smooth atomic background was modeled with a third-degree polynomial function. We interpolated the pre-edge background with a straight line and then extrapolated data with the Lengeler–Heisenberger method (11) to extract the EXAFS signal. Analysis of the L_{III} edge EXAFS spectra of Ce was performed in a similar way, but the background absorption coefficient was modeled with four cubic splines. Analysis of L_{III}-edge EXAFS spectra of Ce presented here is limited to the first-shell contribution.

2.2.1. Zr K edge. To separate the different atomic shell contributions present in the EXAFS signal, we performed a Fourier transform of the k^3-weighted EXAFS signal convoluted with a Kaiser apodization window ($\tau = 2.5$). The fast Fourier transform (FFT) was performed in the interval 3.0–12.7 Å^{-1}. In Fig. 1 we show k-weighted EXAFS signals and the Fourier transform. Modelizations of signals were performed on back-transformed intervals of the FFT. We recognized in FFT-transformed signals of every sample two fundamental contributions: in the interval 1.1–2.3 Å a first peak due to oxygen first neighbors; then in the interval 2.3–4.2 Å a second peak due to convoluted signals of second (i.e., metal) and third (i.e., oxygen) neighbors. Values of interval limits changed slightly from one sample to another.

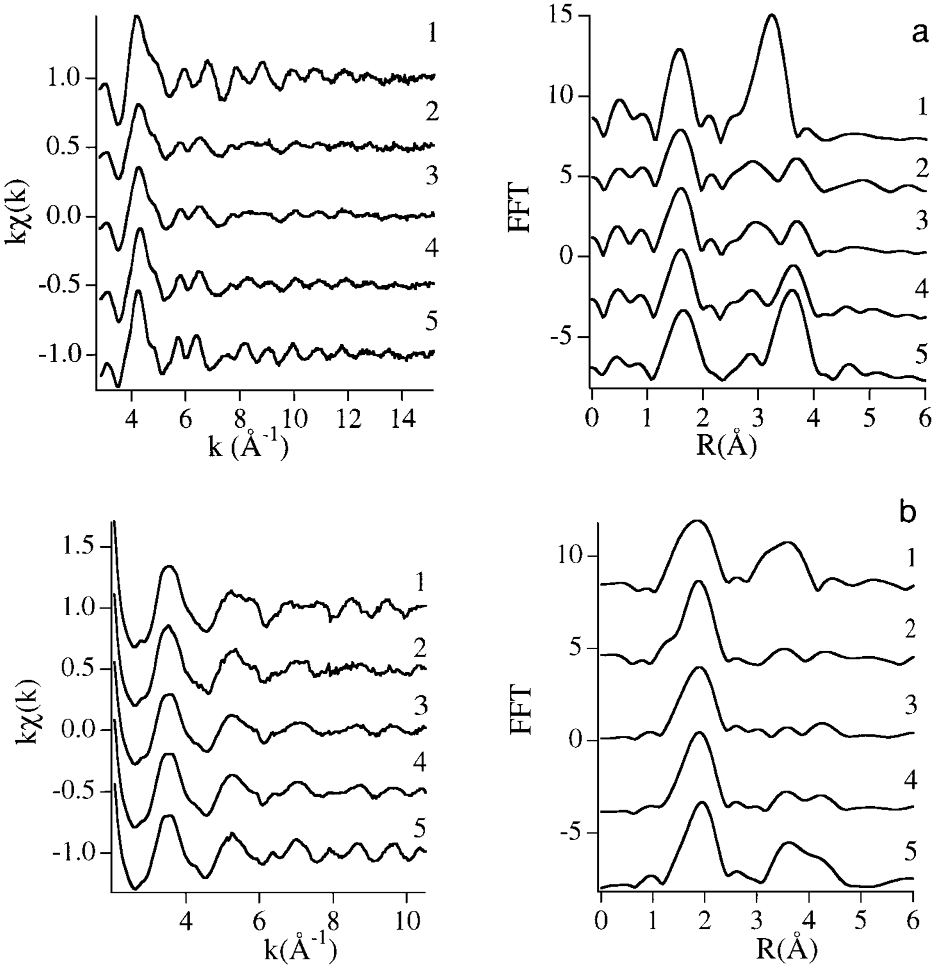

FIG. 1. k-weighted EXAFS spectra (left) and their FFTs (right) for (a) Zr K edge and (b) Ce L_{III} edge: (1) t-$Ce_{0.2}Zr_{0.8}O_2$, (2) t'-$Ce_{0.5}Zr_{0.5}O_2$, (3) t''-$Ce_{0.5}Zr_{0.5}O_2$, (4) t''-$Ce_{0.6}Zr_{0.4}O_2$, (5) c-$Ce_{0.8}Zr_{0.2}O_2$.

We used experimental phase and amplitude functions for the Zr–O atom pair to model first peak signal, using $BaZrO_3$ as standard. The nearest neighbors (NNs) to Zr in this compound are six oxygen atoms at an average distance of 2.09 Å (12). As a definition of a relative scale of σ was needed, we chose for this standard the arbitrary value $\sigma = 0.07$ Å; all other values of σ for the Zr–O couple are in proportion to this.

To simulate the second peak signal we used theoretical functions of McKale *et al.* (13) since no standard for Zr–Ce is available. We tested the McKale *et al.* functions for the Zr–Zr atom pair on Zr metal: we fixed the distance to the crystallographic value and the disorder term to the value calculated at the temperature of 293 K with the model of Sevillano *et al.* (14). We obtained a very good simulation of the Zr–Zr EXAFS FFT-filtered signal and we could estimate the value of the Γ coefficient (0.89 Å^{-2}). This value is necessary to calculate the mean free path with the simplified empirical expression proposed by Lee (15):

$$\lambda(k) = k\Gamma^{-1}.$$

This value of the mean free path parameter was then used in the simulation of the second peak of other samples.

All refinements were performed on k-weighted filtered data. We used mean standard deviations of at least three k-weighted EXAFS data to calculate χ^2 during fitting procedures. We calculated error bars by standard formulas based on inversion of the Hessian matrix. The formula for the number of independent points is (16)

$$N_{\text{ind}} = 2\Delta k \Delta R/\pi + 2,$$

where Δk is the interval in k space on which the fit is performed and ΔR is the back-Fourier transform interval. We define the degree of freedom of the fit as $\nu = N_{\text{ind}} - N_{\text{par}}$, where N_{par} is the number of free parameters used.

Due to the different standards available we used different fit strategies for the first and second peaks. With respect to the first peak we investigated the structure of the oxygen shell to define which was the most probable model. We were concerned with precisely determining distances and coordination numbers. To obtain these results, we carefully used the fitting parameters, decreasing the degree of freedom only when it was strictly necessary and physically meaningful. In fact we found that it was impossible to properly simulate the first peak by means of only one Zr–O distance. We had to use at least two shells of oxygen around a zirconium atom, so the number of fitting parameters increased and the possibility of producing false results grew considerably. As recently pointed out, in the presence of multiple minima in the merit function, the use of different ΔE values to simulate the scattering contributions of equal scattering atoms located at similar distances may lead to identification of a chemically unreliable solution (17). To avoid these problems, we systematically used equal ΔE values for the same kind of scattering atom.

The second peak in the FFT contains the contributions of the metal neighbors [next nearest neighbours (NNNs)] and the second oxygen neighbors. Here different ΔE_0 values for different shells could be necessary to count for different oxidation states and distances between the theoretical standards and the samples. For this reason the fit strategy was different: we started refining only the contributions of the metal atoms and limiting the k range between 6 and 12.7 Å^{-1}, so all ΔE_0 parameters were assigned the same value. Then we introduced the contribution of the oxygen atoms and we used a wider range: from 3.0 to 12.7 Å^{-1}. In this step the ΔE_0 parameters of the three shells were still kept equal. Starting from the minimum found in this step, we allowed the ΔE_0 parameters to have different values. In almost all cases the values of ΔE_0 varied only slightly. In any case the ΔE_0 correction was less than 3 eV. For this reason we present here only the data obtained with the same ΔE_0 for all three shells. We used only one distance to simulate the second oxygen neighbors; this is not coherent with the results of the first peak analysis, but this simplification is due only to the limited number of independent points. On the other hand, the oxygen shells in the second peak have a limited weight and can be well approximated by a single shell with a large disorder factor. In fact we obtained high values for the disorder factor of the oxygen shell (i.e., ∼0.14 Å).

2.2.2. Ce L_{III} edge. The k^3-weighted EXAFS signals of the Ce L_{III} edge were Fourier transformed in the interval 2.41–9.85 Å^{-1} and the first peak contribution was filtered in the interval 1.02–2.46 Å. The k-weighted EXAFS signals and their FFTs are shown in Fig. 1b. To fit the data we chose CeO_2 as standard. The data used to calculate the scattering phase and amplitude are $R = 2.341$ Å, $\sigma = 0.07$ Å, $\Gamma = 1.0$, CN = 8. In all samples single-shell calculations were sufficient to simulate the first peak signal.

3. RESULTS

3.1. Oxygen Exchange Properties (Reduction Behavior)

The reduction behavior and catalytic activity of the reduction of NO with CO of the present catalysts were reported previously (6, 7, 9). For the reader's convenience, these data are described in brief here. Reduction of highly sintered Rh/CeO_2 features two peaks at 380 and 1110 K. The peak below 500 K is attributed to reduction of the rhodium oxide precursor, while the peak at 1110 K is attributed to reduction of CeO_2 in the bulk. No evidence of CeO_2 surface reduction processes is found due to the sintered nature of the catalyst. The modification of the reduction profile by insertion of ZrO_2 into the CeO_2 lattice is striking as illustrated by the formation of a new peak at about 600–700 K (Fig. 2). The position of this new low-temperature (LT)

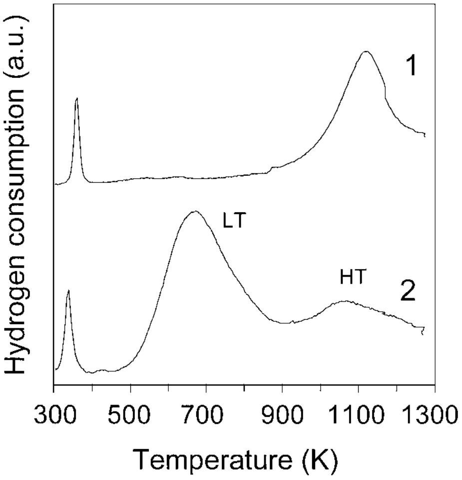

FIG. 2. Temperature-programmed reduction profiles of Rh/CeO_2 and $Rh/Ce_{0.6}Zr_{0.4}O_2$.

reduction peak depends both on the nature of the CeO_2–ZrO_2 phase and on CeO_2 content. This is illustrated in Fig. 3. For a full discussion of these features we refer the reader to Ref. (7). Concerning the present paper, the following features should be noted: (i) due to the low surface area of the samples employed here the LT peak is associated with reduction in the bulk of the CeO_2–ZrO_2 mixed oxide promoted by ZrO_2; (ii) the extent of the promotional effect increases with ZrO_2 content at the CeO_2-rich side (cubic phase) and it decreases at the ZrO_2-rich side (tetragonal phases). These observations suggest that the facility of the reduction should be associated with the ease of oxygen migration in the bulk of the mixed oxide (7).

3.2. *XRD and Raman Characterization*

According to the cerium content, ceria–zirconia ceramic alloys exist in three different phases, namely, monoclinic, tetragonal, and cubic (18). Below 1300 K the monoclinic and cubic phases appear to be thermodynamically stable; however, when the ceramic method is employed for synthesis of the solid solution the metastable tetragonal phase is easily formed in a wide compositional interval and it is fairly stable at ordinary temperatures (19–23). In our synthesis we used a nonquenching cooling rate which produces two phases of tetragonal symmetry referred to as t and t' (20–23). These phases exist pure in the compositional ranges 5–20% CeO_2 and 40–60% CeO_2, respectively, while at a CeO_2 content of 20–40% a mixture of t and t' is obtained. The former phase is characterized by a larger orthogonality ($c/a = 1.018$) compared with the t' phase ($c/a \sim 1.010$) (24). Recently, a tetragonal t'' phase was distinguished on the basis of the Raman spectra. This phase is characterized by a cation sublattice of $Fm3m$ symmetry and a tetragonal ($P4_2/nmc$ space group) distortion of the oxygen sublattice (20). Since the XRD patterns are sensitive mainly to the cation sublattice, the c and t'' phases are often referred to as a cubic phase. This term will also be used here.

Some representative powder XRD patterns are shown in Fig. 4. As shown in trace 4, the XRD profiles suggest that formation of a cubic fluorite-type solid solution occurred for cerium contents >50 mol%. For the composition $Ce_{0.5}Zr_{0.5}O_2$, both tetragonal and cubic phases may be obtained according to the synthesis conditions. Quick quenching to RT of the calcined mixture produces the cubic phase,

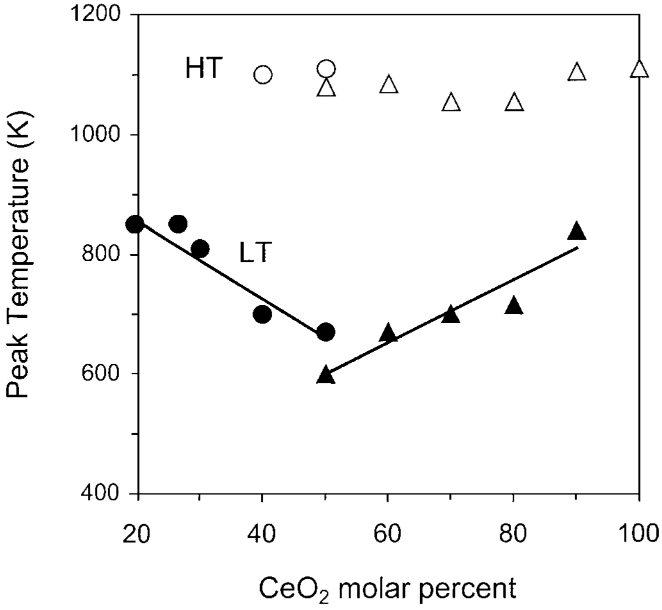

FIG. 3. Temperatures of the LT and HT peaks versus CeO_2 content: (●, ○) tetragonal (t, t') and (▲, △) cubic (t'', c) phases.

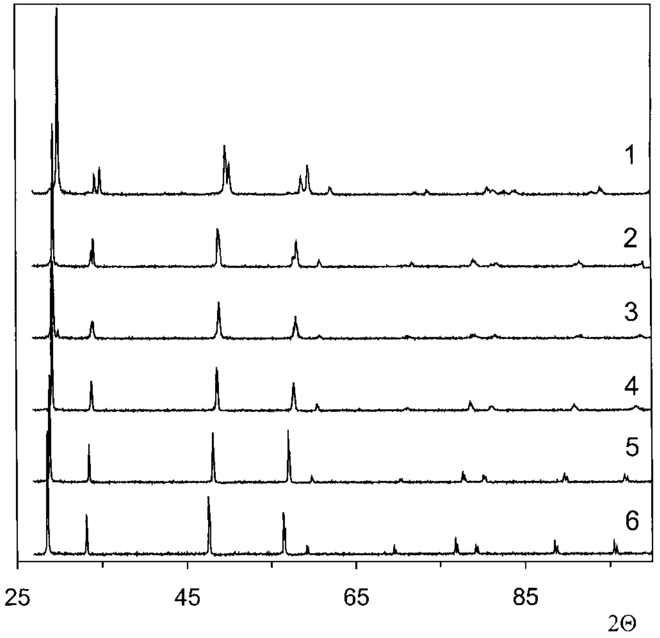

FIG. 4. Powder XRD spectra of (1) t-$Ce_{0.2}Zr_{0.8}O_2$, (2) t'-$Ce_{0.5}Zr_{0.5}O_2$, (3) t''-$Ce_{0.5}Zr_{0.5}O_2$, (4) t''-$Ce_{0.6}Zr_{0.4}O_2$, (5) c-$Ce_{0.8}Zr_{0.2}O_2$, and (6) CeO_2.

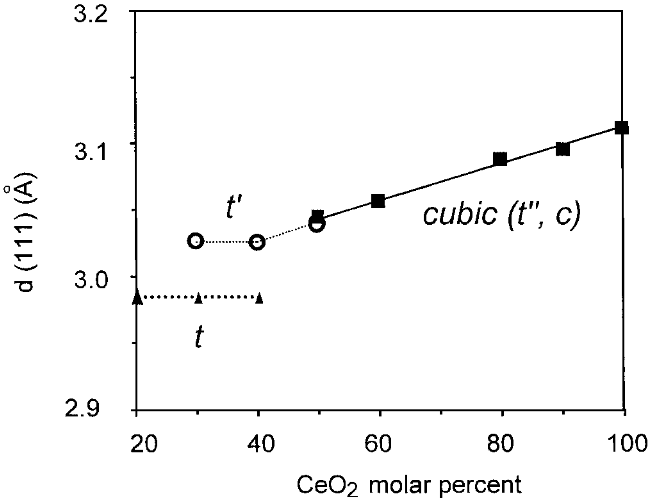

FIG. 5. (111) spacing of CeO_2–ZrO_2 solid solutions as determined by powder XRD.

while slow cooling leads to the t' phase as detected by the splitting of the peaks at about 32°, 48°, and 57° 2θ. As shown in Fig. 5, powder XRD spectra confirmed formation of solid solutions in the present samples. In agreement with the Vegard rule, $d(111)$ decreases linearly in the cubic region with decreasing CeO_2 content due to the smaller ionic radius of Zr^{4+} (0.80 Å) compared with Ce^{4+} (0.97 Å). In the range of composition 30–40% CeO_2, the constant values of (hkl) spacing indicate that a two-phase region is present as expected on the basis of the phase diagram. Consistently, both $Ce_{0.3}Zr_{0.7}O_2$ and $Ce_{0.4}Zr_{0.6}O_2$ are mixtures of respectively t (77 and 22%), t' (17 and 67%), and cubic (6 and 11%). All other samples present a single phase.

Due to the low sensitivity of the XRD technique to the oxygen sublattice, Raman spectra were collected in the range 100–1000 cm^{-1} where absorption due to M–O stretching is observed. The overall picture, reported in Fig. 6, indicates substantial modification of M–O bonding symmetry on variation of CeO_2 content.

Six Raman-active modes of $A_{1g} + 3\,E_g + 2\,B_{1g}$ symmetry are observed for tetragonal ZrO_2 (space group $P4_2/nmc$), while for the cubic fluorite structure (space group $Fm3m$) only one F_{2g} mode centered at around 490 cm^{-1} is Raman-active (25). In pure CeO_2 ($Fm3m$ space group), the F_{2g} mode is observed at 465 cm^{-1}. The Raman spectra reported in Fig. 6 show the following features: (i) For CeO_2 contents above 60 mol%, the spectrum is dominated by a single strong band which shifts to higher frequencies and becomes sharper with increasing CeO_2 content. This band is attributed to the F_{2g} mode. Also, some minor peaks at about 310 and 145 cm^{-1} are noted. (ii) At high ZrO_2 content ($\geq$80 mol%) the six bands of tetragonal ZrO_2 are detected. (iii) At intermediate CeO_2 contents (40–60 mol%), four or five bands are detected.

The shift in the Raman frequency to higher values with increasing ZrO_2 content is due to the decrease in the lattice parameter, resulting in short M–O bond lengths. Note that peaks at 310 and 145 cm^{-1} are also observed. Such spectral features were attributed to the t'' phase (20, 21). Observation of only four or five Raman modes for the intermediate CeO_2 contents cannot be rationalized on the basis of the proposed phase symmetries ($P4_2/nmc$ and $Fm3m$). It suggests that additional modifications of the oxygen sublattice may occur at this intermediate CeO_2 level. In fact at high

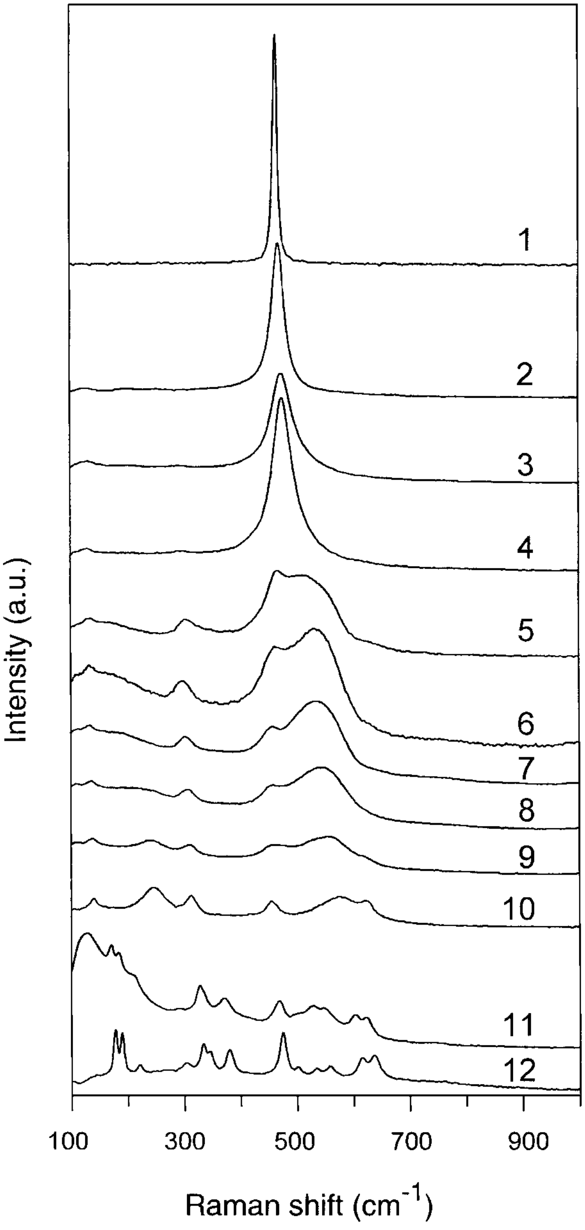

FIG. 6. Raman spectra of $Ce_xZr_{1-x}O_2$: x = (1) 1, (2) 0.9, (3) 0.8, (4) 0.7, (5) 0.6, (6) 0.5—t' phase, (7) 0.5—t'' phase, (8) 0.4, (9) 0.3, (10) 0.2, (11) 0.1, and (12) 0.

TABLE 1

XRD Characterization of $Ce_xZr_{1-x}O_2$[a]

CeO_2 (mol%)	Cubic phase	t' phase		t phase	
	$a=b=c$ (Å)	$a'=b'$ (Å)	c (Å)	$a'=b'$ (Å)	c (Å)
100	5.407				
90	5.379				
80	5.353				
70	5.350				
60	5.301				
50	5.274				
50		5.260	5.304		
40	5.298	5.224	5.284	5.142	5.241
30	5.319	5.224	5.284	5.142	5.241
20				5.151	5.239

[a] a', b', and c' (with $a'=b'=a\sqrt{2}\,ec'=c$) are the cell parameters of the double tetragonal cell.

ZrO_2 contents (ii), 6 bands are observed allowing attribution to the t phase.

The phase attribution and structural parameters as detected from the XRD patterns are summarized in Table 1.

3.3. *EXAFS Characterization*

On the basis of the Raman and XRD characterization, five single-phase samples—t-$Ce_{0.2}Zr_{0.8}O_2$, t'-$Ce_{0.5}Zr_{0.5}O_2$, t''-$Ce_{0.5}Zr_{0.5}O_2$, t''-$Ce_{0.6}Zr_{0.4}O_2$, and c-$Ce_{0.8}Zr_{0.2}O_2$—were analyzed by the EXAFS technique. Both the Zr K and Ce L_{III} edges were measured and the results are described in the following sections.

3.3.1. Zr K edge. The simulation of contribution to the EXAFS signal of oxygen NNs was carried out by testing a number of different models (8). The statistical discrimination was made on the basis of the F test requiring a probability of at least 75% (8). However, before discussing the data, which concern the CeO_2–ZrO_2 mixed oxides, it is important to examine the results of fitting for the reference model compound m-ZrO_2. Zr atom in monoclinic ZrO_2 is surrounded by seven oxygen atoms at seven different distances: 2.051, 2.057, 2.151, 2.163, 2.189, 2.220, and 2.285 Å (26). They can be grouped in different ways to reduce the number of fitting parameters. A number of models and the average crystallographic distances are reported in Table 2. The single-shell model can be clearly distinguished with respect to the others on the basis of the χ^2 factor; however, it is interesting to note that a correct CN is obtained by leaving free the CN parameter during the fitting. By keeping ΔE_0 constant, the three-subshell model (model 3, Table 2) best fits the XRD data. In fact on the basis of the F-test, the three-shell model is 75% more probable than the two-shell model (model 2) and 70% more probable than the one-shell model (model 1). Remarkably, by leaving the ΔE_0 independent for the two subshells (model 4), we obtained a fit that is statistically indistinguishable from the three-shell fit obtained using single ΔE_0. Note, however, that the second distance differs by 0.03 Å from the average value of the crystallographic data. In addition, the difference between the two ΔE_0 values exceeds 3 eV. Both these arguments make this model physically unreliable, despite the very satisfactory fit. In Fig. 7 we show average EXAFS signals of monoclinic ZrO_2 and its FFT transform (both modulus and imaginary part); we show also (in dashed line) the theoretical Fourier transform of the three-shell model function (model 3).

Good agreement between the experimental data and the fit is observed. In summary, analysis of the Zr–O shell in ZrO_2 confirms the validity of our approach in fitting Zr–O, i.e., using a single value of ΔE_0 for all the oxygen subshells. Accordingly, we systematically employed this approach to

TABLE 2

Results of Fitting the EXAFS Signal by Using Different Models for the First Shell of Monoclinic ZrO_2 Compared with the Crystallographic Data

	EXAFS						XRD	
Model	CN[a]	σ (Å)	Distance (Å)	ΔE_0 (eV)	χ^2	ν	CN	Average distance (Å)
1	7.2 ± 0.2	0.102 ± 0.003	2.142 ± 0.004	−0.2 ± 0.2	3.77	4	7	2.159
2	5	0.078 ± 0.005	2.114 ± 0.003	−0.2 ± 0.2	2.81	4	5	2.120
	2		2.25 ± 0.01				2	2.250
3	2	0.04 ± 0.01	2.049 ± 0.007	0.1 ± 0.2	1.40	3	2	2.054
	3		2.154 ± 0.005				3	2.168
	2		2.27 ± 0.01				2	2.250
4	5	0.080 ± 0.005	2.113 ± 0.003	−0.6 ± 0.4	1.83	3	5	2.120
	2		2.28 ± 0.01	2.4 ± 1.2			2	2.250

[a] Coordination number.

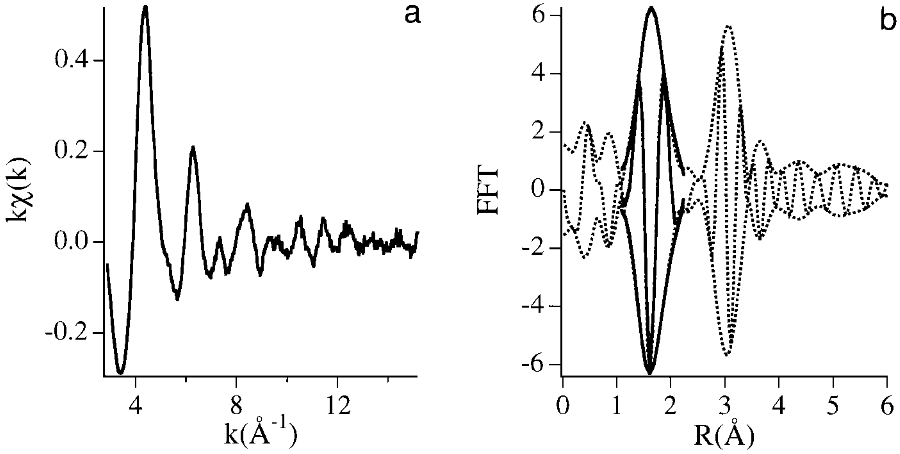

FIG. 7. *k*-weighted EXAFS spectra of monoclinic ZrO_2 (a) and its FFT (b) with simulated FFT of first peak obtained using model 3. —, fit; ---, experimental.

fit the Zr–O shell of all the samples. An example of the fitting is reported for *t*-$Ce_{0.2}Zr_{0.8}O_2$ in Fig. 8. Similar results were obtained for all the other samples.

A perusal of data reported in Table 3 reveals that (i) a single shell of oxygen NN atoms to Zr has never been detected for any of the CeO_2–ZrO_2 oxides investigated, and (ii) the oxygen shell structure depends on the amount of ZrO_2 inserted into the CeO_2 lattice. In the $Ce_{0.2}Zr_{0.8}O_2$ sample, zirconium appears eight coordinated, with two possible models for the oxygen shells. Actually we observed that the two models are equivalent. In fact, the second and third shells of the $4+2+2$ model are simply approximated by the second shell in the case of the $4+4$ model. The sum of the square of the distance dispersion of the last two shells of the $4+2+2$ model and their disorder parameters almost equals the square of the disorder parameters of the second shell in the $4+4$ model. The $4+4$ model is consistent with the presence of a tetragonal phase.

When the cerium content increases (50–80 mol%), the coordination number of zirconium changes. The appropriate model for the cubic samples is $4+2$. The coordination number decreases by 2 units with respect to $Ce_{0.2}Zr_{0.8}O_2$. Due to the increase in the cell parameter, the outer shell of the oxygen atoms could move too far to be localized by EXAFS analysis in the first peak of the FFT. In fact its contribution could be mixed and confused with those of heavier atoms in the intermediate region between the first and second peaks.

In the case of tetragonal $Ce_{0.5}Zr_{0.5}O_2$ we obtained a minimum for the coordination number of zirconium; its value is near 5 and should not be confused within the experimental error (±10%) with 6.

The Zr–O bond distances increase along the series; this is true for all the peaks analyzed and is in agreement with XRD data. The disorder parameter decreases in the cubic samples, indicating a less distorted oxygen lattice as the

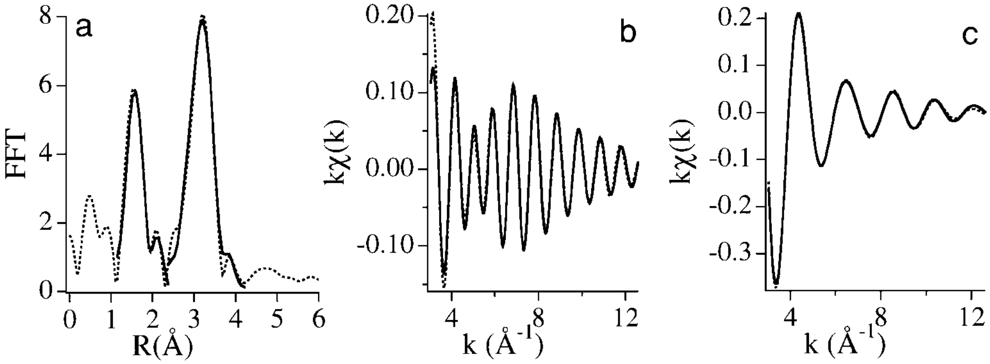

FIG. 8. Fitting of EXAFS data at the Zr *K* edge for *t*-$Ce_{0.2}Zr_{0.8}O_2$: (a) Modulus of the FT of the experimental data and the modeled FTs relative to the first and second shells (*R* space); (c) back-FT of the first peak and the corresponding fit; (b) back-FT of the second peak and the corresponding fit (*k* space). —, fit; ---, experimental.

TABLE 3

Results of Fitting of the EXAFS Signal at the Zr K Edge: Zr NN Shell

Sample	CN[a] Zr–O	σ (Å × 10^{-2})	R (Å)	ΔE_0 (eV)	χ_ν^2	ν
t-$Ce_{0.2}Zr_{0.8}O_2$	4	6.2 ± 0.5	2.086 ± 0.004	0.4 ± 0.2	0.50	4
	2	6.2 ± 0.5	2.240 ± 0.007	0.4 ± 0.2		
	2	6.2 ± 0.5	2.39 ± 0.01	0.4 ± 0.2		
	4	6.3 ± 0.6	2.089 ± 0.006	0.4 ± 0.4	0.69	4
	4	10 ± 1	2.301 ± 0.01			
t'-$Ce_{0.5}Zr_{0.5}O_2$	3	6.5 ± 0.4	2.117 ± 0.005	2.1 ± 0.2	3.02	5
	2	6.5 ± 0.4	2.325 ± 0.008	2.1 ± 0.2		
t''-$Ce_{0.5}Zr_{0.5}O_2$	4	8.0 ± 0.3	2.124 ± 0.006	0.9 ± 0.4	1.94	5
	2	8.0 ± 0.3	2.34 ± 0.01	0.9 ± 0.4		
t''-$Ce_{0.6}Zr_{0.4}O_2$	4	7.6 ± 0.3	2.134 ± 0.003	1.1 ± 0.2	1.36	5
	2	7.6 ± 0.3	2.328 ± 0.008	1.1 ± 0.2		
c-$Ce_{0.8}Zr_{0.2}O_2$	4	6.9 ± 0.3	2.164 ± 0.003	1.0 ± 0.2	7.94	6
	2	6.9 ± 0.3	2.329 ± 0.006	1.0 ± 0.2		

[a] Coordination number.

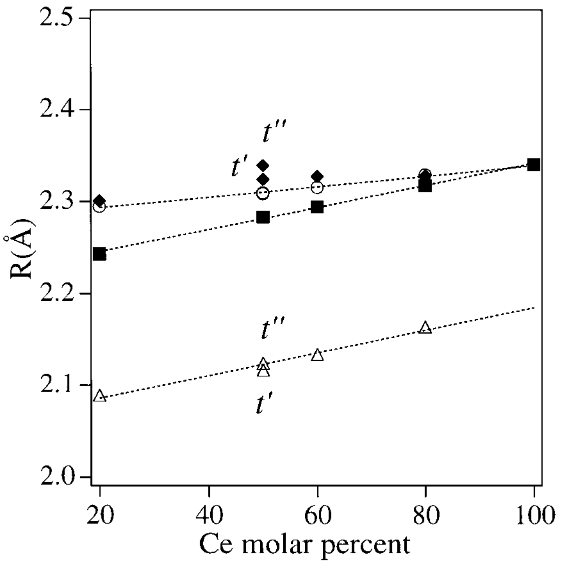

FIG. 9. Comparison of Ce–O (○), Zr–O (first subshell, △; second subshell, ◆) distances obtained by EXAFS and metal-oxygen distances deduced by XRD cell parameters (■) assuming cubic or tetragonal symmetry.

cerium content increases. The tetragonal samples show less dispersion of Zr–O bonds compared with the cubic samples, suggesting a more ordered oxygen sublattice.

Data obtained for the Zr NNNs are reported in Table 4. These data were obtained by fitting the contribution of the second series of peaks shown in the FFT in the range 2.3–4.2 Å (Fig. 1). This region is associated prevalently with M–M bonding and some oxygen contribution. As expected, at both ends of the investigated compositions (Zr contents 20 and 80 mol%), a single peak prevails, while for intermediate compositions two peaks, related to Zr–Zr and Zr–Ce bonding, are observed. It is also noted that the amplitude of the signal of the two contributions to the second FFT peak decreases when approaching a molar Ce/Zr ratio equal to 1. This phenomenon, which could suggest a high structural disorder and/or decrease in CN, is due to the mixing of the Zr and Ce phases that differ with respect to π on almost all the used wavevector domain. This produces a destructive interference that tends to wipe out the second FFT peak. This is also evident from the fitting results: the Debye–Waller

TABLE 4

Results of Fitting of the EXAFS Signal at the Zr K Edge: Zr NNN Shell

Sample	Shell	CN[a]	σ (Å × 10^{-2})	R (Å)	ΔE_0 (eV)	χ_ν^2	ν
t-$Ce_{0.2}Zr_{0.8}O_2$	Zr–Zr	9.6	8.0 ± 0.3	3.628 ± 0.007	−8.7 ± 0.7	5.37	6
	Zr–Ce	2.4	7.0 ± 0.7	3.66 ± 0.01	−8.7 ± 0.7		
	Zr–O	24	13.4 ± 0.6	4.19 ± 0.03	−8.7 ± 0.7		
t'-$Ce_{0.5}Zr_{0.5}O_2$	Zr–Zr	6	10.7 ± 0.4	3.661 ± 0.008	−6.9 ± 0.3	1.94	6
	Zr–Ce	6	9.6 ± 0.3	3.718 ± 0.007	−6.9 ± 0.3		
	Zr–O	24	15.4 ± 0.5	4.29 ± 0.01	−6.9 ± 0.3		
t''-$Ce_{0.5}Zr_{0.5}O_2$	Zr–Zr	6	10.2 ± 0.3	3.659 ± 0.007	−7.0 ± 0.3	1.98	6
	Zr–Ce	6	9.3 ± 0.3	3.719 ± 0.006	−7.0 ± 0.3		
	Zr–O	24	14.4 ± 0.4	4.28 ± 0.01	−7.0 ± 0.3		
t''-$Ce_{0.6}Zr_{0.4}O_2$	Zr–Zr	4.8	10.2 ± 0.3	3.674 ± 0.007	−7.4 ± 0.2	9.63	5
	Zr–Ce	7.2	8.9 ± 0.2	3.729 ± 0.005	−7.4 ± 0.2		
	Zr–O	24	12.9 ± 0.4	4.300 ± 0.008	−7.4 ± 0.2		
c-$Ce_{0.8}Zr_{0.2}O_2$	Zr–Zr	2.4	11.1 ± 0.6	3.66 ± 0.01	−6.1 ± 0.1	16.72	7
	Zr–Ce	9.6	9.3 ± 0.1	3.771 ± 0.002	−6.1 ± 0.1		
	Zr–O	24	9.9 ± 0.2	4.362 ± 0.003	−6.1 ± 0.1		

[a] Coordination number.

factors of the Zr–Ce, Zr–Zr, and Zr–O pairs do not change so much to produce such a dumping of the signals. Accordingly we did not find any significant change in NNN CNs as the Ce/Zr ratio was varied. The alloying between Zr and Ce oxide with formation of a homogeneous solid solution was discussed in a previous paper (9). Here we confirm that for all the compositions investigated, the EXAFS data at the Zr *K* edge cannot be modeled without introducing the cerium contribution with appropriate stoichiometry. One should, however, be aware that the amplitude accuracy of EXAFS analysis (±10%) would not allow detecting partial/limited segregation in the phases.

The average Zr–Zr, Zr–Ce, and Zr–O distances increase with the Ce content, in agreement with the occurrence of alloying and formation of a solid solution. This is substantiated by the comparison of the EXAFS data with the calculated (XRD) Zr–Ce distances on the assumption that the cations statistically occupy special positions of the tetragonal/cubic lattice. There is good agreement on the whole composition interval, also confirming the validity of the EXAFS analysis (Fig. 10). Similarly, Zr–O second-shell distance increases with CeO_2 content. In contrast, Zr–Zr distance seems to be almost unaffected by the alloying. At present, this is hardly explained as a real structural effect; future investigation is needed to solve the problem.

In agreement with the results for the first oxygen shell, the disorder parameter of the NNN oxygen shell is highest for the tetragonal samples and lowest at the highest cerium content. This indicates that the dispersion of oxygen distances decreases in the cubic phase, as the structure becomes more and more similar to the highly symmetric structure of CeO_2. The fact that the maximum corresponds to the tetragonal $Ce_{0.5}Zr_{0.5}O_2$ sample is consistent with the observations done for the first peak analysis. In fact, we suggest that due to the difficulty of identifying the outer oxygen shell for distances equal to or higher than 2.5 Å by the EXAFS technique, we found a low coordination number. Thus, we observe only five oxygen atoms in the first peak of the tetragonal sample, which implies a high dispersion of oxygen bond distances.

3.3.2. Ce L_{III} edge. The results obtained at the Ce L_{III} edge are shown in Table 5. In all cases the coordination number of Ce is near eight, in contrast with the results for the Zr first shell (Table 3). No evidence of splitting in more shells of the first oxygen neighbors was ever found. Comparison of the Ce–O bond distances with those obtained from the XRD cell parameters is in good agreement with EXAFS data (Fig. 9), the Ce–O distance increasing with CeO_2 molar percentage.

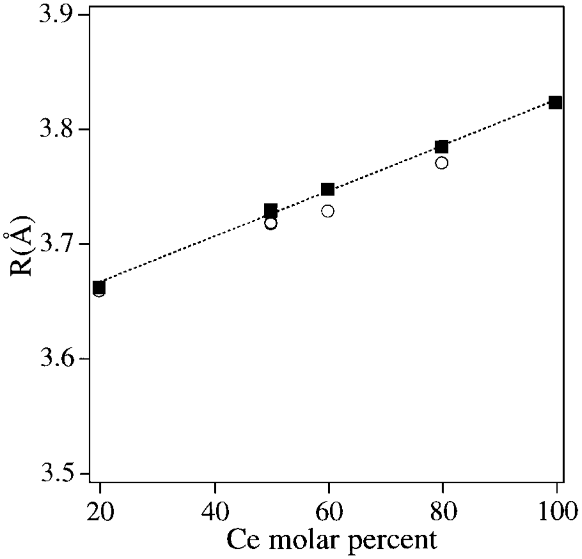

FIG. 10. Comparison of Ce–Zr distances obtained by EXAFS (○) and metal–metal distances deduced by XRD data (■) assuming cubic or tetragonal symmetry.

4. DISCUSSION

The first point to be addressed is whether the present mixed oxides can be addressed as truly homogeneous solid solutions. The linear variation of the cell parameter as detected by $d(111)$ in the XRD spectra and lack of evidence of the presence of the starting materials clearly suggested that the solid-state synthesis employed here leads to formation of solid solutions. Their homogeneity is supported by the EXAFS data which showed a good correlation between the mixed oxide composition and Zr–M (Ce or Zr) bond structure. The consistency of the Debye–Waller (DW) factor in

TABLE 5

Results of Fitting of the EXAFS Signal at the Ce L_{III} Edge: Ce NN Shell

Sample	CN[a] Ce–O	σ (Å × 10^{-2})	R (Å)	ΔE_0 (eV)	χ^2_ν	ν
t-$Ce_{0.2}Zr_{0.8}O_2$	8.5 ± 0.2	8.9 ± 0.4	2.295 ± 0.003	0.6 ± 0.1	0.51	5
t'-$Ce_{0.5}Zr_{0.5}O_2$	7.8 ± 0.8	7.5 ± 0.8	2.31 ± 0.01	-0.7 ± 0.7	0.21	5
t''-$Ce_{0.5}Zr_{0.5}O_2$	7.8 ± 0.2	8.6 ± 0.3	2.309 ± 0.003	-0.7 ± 0.1	2.40	3
t''-$Ce_{0.6}Zr_{0.4}O_2$	8.7 ± 0.2	8.7 ± 0.2	2.316 ± 0.002	-0.5 ± 0.1	4.31	4
c-$Ce_{0.8}Zr_{0.2}O_2$	8.5 ± 0.1	8.2 ± 0.2	2.330 ± 0.001	-0.2 ± 0.1	10.42	4

[a] Coordination number.

the mixed oxides and ZrO_2 is a further indication of homogeneity. For a domain-type structure, as often suggested for these materials, one would expect a high DW factor for the Zr–M bond, due to the fact that the local cell parameter in the hypothetical Zr-rich and Ce-rich domains should be rather different, resulting in high DW factors.

Structural analysis of the present CeO_2–ZrO_2 mixed oxides disclosed a number of unprecedented observations concerning the local M—O structure. First, while Ce^{4+} is the chemically active site for redox activity of CeO_2–ZrO_2 mixed oxides as no appreciable Zr reduction could be detected (6, 7), the presence of zirconia in the CeO_2 lattice seems to be responsible for strong modifications of the oxygen sublattice. Let us focus our attention first on the effects of zirconia addition on evolution of the Ce–O bond. These modifications appear to be related to ZrO_2 content in a straightforward manner: An increase in ZrO_2 content leads to progressive shortening of the Ce–O bond. This is consistent with a decrease in the cell parameter, which occurs on substitution of the large Ce^{4+} by the small Zr^{4+}. The linear dependency of $d(111)$ and the results of EXAFS characterization of the Zr–Ce shell strongly suggest that all the single-phase samples are truly homogeneous solid solutions. Detection of a single Ce–O coordination shell clearly indicates that in these systems, cerium maintains its coordination integrity with respect to the fluorite structure of the parent CeO_2. Conservation of this integrity is supported by the Raman spectra in the CeO_2-rich region. The strong intensity of the F_{2g} mode and the linear shift of its frequency with CeO_2 content indicate that Ce–O bond stretching is the major contribution to this mode. The increasing width of the band due to the F_{2g} mode with ZrO_2 content in the cubic region is worthy of comment. In pure CeO_2 variation of the width of the F_{2g} Raman mode was detected and shown to depend linearly on CeO_2 particle size: at lower particle sizes of CeO_2, sharper peaks were observed (27). This modification of the Raman spectra was related to an increase in order of the CeO_2 particles as their size increases. In our case, due to the synthesis method, sintered materials with high particle sizes were obtained. Accordingly, variation of the bandwidth cannot be related to a variation in particle size. In view of the EXAFS characterization, it appears reasonable to associate this modification to an increased structural disorder of the solid solution with increasing content of ZrO_2. Breaking of long-range ordering of the oxygen lattice in the solid coupled to a defect-induced first-order Raman effect was shown to be responsible for the line broadening of the T_{2g} mode in the FSZs[2] (28). Consistently, density measurements suggested the presence of increasing amounts of defects in these solids (7). As yet we have not been able to determine the real nature of these defects; however, as cerium is present in the Ce^{4+} state in all the mixed oxides (29), substantial amounts of oxygen vacancies due to reducible cerium should be excluded. Accordingly, the presence of these defects should rather be associated with the presence of zirconia. This interpretation is substantiated by the observed modification of the Ce–O bond: there is nice agreement between the Ce–O bond lengths as detected by both XRD and EXAFS and this confirms the idea that cerium prefers to conserve its ideal fluorite situation also in the mixed oxide. We recall that the XRD bond lengths are calculated by assuming that both the metal cations and the oxygen anions are located in special positions and no distortion in the oxygen sublattice occurs. Of course, as the amount of the CeO_2 in the mixed oxides decreases, the intensity of the Raman signal relative to cerium bonding also decreases, making the contribution of the Zr–O vibrations prominent. It is also worth noting that the DW factors of the Ce–O bond are relatively constant over the whole range of compositions studied, in agreement with a "constant" situation around cerium in the lattice. Detection of an "ordered" structure around cerium may suggest that the high-temperature peak observed in the TPR profiles could somehow be related to this local situation where removal of oxygen should be difficult and reduction temperatures comparable to those found for pure CeO_2 (1100 K). In fact, we observed that by increasing ZrO_2 content in the cubic region, not only did the LT peaks shift to low temperatures, but also the relative intensity of the HT peaks decreased (7). Further, the decrease in Ce–O bond length should make removal of oxygen bonded to cerium cations more difficult.

As far as the local structure around zirconium is concerned, we find evidence of strong dependency of the local structure on ZrO_2 content and hence the phases present. However, let us first briefly discuss Zr–O in pure zirconia, which, obviously, is the related reference material. At RT, monoclinic Zr–O is stable, unless extremely very fine particles have been produced in the synthesis which lead to stabilization of tetragonal or even cubic phases (25, 30). Three Zr–O bond distances were determined in monoclinic ZrO_2 (Table 2). The data reported in Table 2 are in a good agreement with the crystallographic values, indicating that our experimental approach to treating the EXAFS data gives reliable results. In tetragonal zirconias a CN of 4+4 was detected as predicted by the $P4_2/nmc$ space group. Typically the distances for the two subshells are around 2.10–2.35 Å according to the nature of the stabilizing cation (31–33). Such a situation is found only for the $Ce_{0.2}Zr_{0.8}O_2$ samples. The structural parameters appear in good agreement with previous investigations of CeO_2–ZrO_2 mixed oxides with low CeO_2 content (34). The CN 4+4 is clearly confirmed by Raman spectroscopy, which shows six active bands as predicted by the group analysis. The situation in both the t' and cubic phases appears rather different. In all cases we have not been able to model the EXAFS signal by employing a

---

[2] The terms partially stabilized (PSZ) and fully stabilized (FSZ) zirconia are commonly employed to indicate tetragonal and cubic phases, respectively.

CN 4+4 subshell structure. Also, Raman spectra strongly suggest that this coordination is absent in these samples since six modes are no longer detected. Among the more than 40 different models tested, we found that for most of the samples investigated the Zr *K*-edge EXAFS signal can be reasonably fitted only by the $4+2$ model. This immediately gives rise to the following question: Where are the missing oxygens? A reasonable explanation is that these oxygen atoms move far from the scattering Zr atom. In the second shell, in addition to the Ce and Zr cations, 24 oxygen atoms are present which we have modeled by a single-shell contribution. The overall contribution of this shell to the second peak is rather small, making insignificant the contribution of the two missing oxygen atoms.

The modification of the first Zr–O coordination shell is indeed remarkable: as shown in Fig. 9, the contraction of the first 4 NNs is rather significant, suggesting that the oxygens are very close to the Zr^{4+}, shielding it somehow from the other four oxygens. Accordingly, two oxygens are pushed to a longer distance, which is comparable to that of the Ce–O bond. Apparently, eight oxygen atoms around the small Zr cation are overcrowded which favors the release of the stress by moving part of them far from the cation. This generates a tetragonal distortion (t' phase) which is formed as long as ZrO_2 is the structure-directing factor. The increase in CeO_2 content leads to a decrese in the c/a ratio, making the tetragonal distortion unfavorable. In the presence of trivalent dopants, the oxygen vacancies may migrate toward the zirconium, stabilizing a less crowded situation. This has been suggested to be the mechanism of the stabilization of PSZs and FSZs with trivalent dopants (31). Of course, the larger the trivalent cation, the more efficient is the mechanism of stabilization since small trivalent cations can compete for the oxygen vacancy. For tervalent dopants, the mechanism of PSZ and FSZ stabilization is not yet understood (34). Unless a highly reducible cation is employed, the above mechanism of stabilization cannot be operative since no oxygen vacancies are present in the solid. Accordingly, we do not have evidence of significant amounts of Ce^{3+} in the as-prepared catalysts. The only way to release the stress around zirconia is then to increase the structural disorder by moving part of the oxygens away. In agreement we note an increase in the DW from c-$Ce_{0.8}Zr_{0.2}O_2$ to cubic-$Ce_{0.5}Zr_{0.5}O_2$. Differently, in the t'-$Ce_{0.5}Zr_{0.5}O_2$ sample a relatively low DW factor is observed, which is consistent with a relaxation induced by tetragonal distortion of the cation lattice. However, as the c/a ratio is close to 1, a full relaxation and the CN 4+4 coordination are not allowed yet. The unavailability of crystallographically pure phases for cerium contents of 30–40% does not allow to establish how the transition from this tetragonal CN 4+2 distribution to the tetragonal CN 4+4 coordination occurs. However, the observation that for these compositions a biphasic region is present suggests that the driving force for the formation of the *t* phase is very high. This makes the diffusional-type phase separation favorable.

We infer that the displacement of the oxygen far from zirconium is responsible for the promoting effects of zirconia on the reduction behavior of CeO_2. These oxygens appear to be highly disordered in the lattice. In fact we have not been able to detect them even at liquid He temperature (8), suggesting that they are structurally rather than thermally disordered. We guess that highly disordered oxygen should easily float in the lattice, making the reduction in the bulk of the material favorable. The higher the disorder, the higher the reducibility of the mixed oxide as clearly indicated by the comparison of the reduction behavior of t'- and t''-$Rh/Ce_{0.5}Zr_{0.5}O_2$ samples. This is clearly confirmed by the DW factors of these two samples. An important point is to which extent these findings can be extended to rationalize the OSC property of CeO_2–ZrO_2 mixed oxides. In fact, it has been shown that reduction behaviour depends strongly also on textural properties of the solid solutions. Samples of different origin and different texture showed different reduction behavior and even an unusual promotion of reduction behavior with sample sintering has been detected (4, 35). We feel that from the increasing number of published papers some conclusions can perhaps be advanced: CeO_2–ZrO_2 mixed oxides show improved oxygen storage due to the availability of bulk oxygen for redox processes. As indicated in the present study this behavior must be associated with a significant distortion of the oxygen sublattice, which is generated by substitution of the small zirconium cation for cerium. The extent of these modifications depends on several factors and, in particular, the relative CeO_2–ZrO_2 composition. Although not addressed in this paper, sample homogeneity and particle size of the CeO_2–ZrO_2 solid solution strongly affect redox behavior. It seems that in high-surface-area CeO_2–ZrO_2 mixed oxides observation of a single reduction feature can be attributed to the presence of a single phase, the presence of different phases being detected by multiple reduction peaks (36). Also, particle size affects the distortion of the oxygen sublattice as detected by Raman spectroscopy: lower particle size favors a higher symmetry of the M–O bond, suggesting that in the CeO_2–ZrO_2 phase diagram a further dimension should be added, e.g., particle size. Breaking of the M–O bond symmetry, which creates mobile oxygens in the lattice, was indeed indicated as a possible origin of the unusual promotion of reduction behavior on sintering (4).

ACKNOWLEDGMENTS

The University of Trieste, Ministero dell'Ambiente (Rome) (Contract DG 164/SCOC/97) and CNR (Rome) Programmi Finalizzati "Materiali Speciali per Tecnologie Avanzate II" (Contract 97.00896.34) are gratefully acknowledged for financial support.

REFERENCES

1. Degobert, P., “Automobiles and Pollution.” Soc. of Automotive Engineers, Warrendale, PA, 1995.
2. Heck, R. M., and Farrauto, R. J., “Catalytic Air Pollution Control: Comercial Technology.” Van Nostrand Reinhold, New York, 1995.
3. Taylor, K. C., *in* “Catalysis—Science and Technology” (J. R. Anderson and M. Boudart, Eds.), Chap. 2. Springer-Verlag, Berlin, 1984.
4. Fornasiero, P., Balducci, G., Di Monte, R., Kaspar, J., Sergo, V., Gubitosa, G., Ferrero, A., and Graziani, M., *J. Catal.* **164**, 173 (1996).
5. Murota, T., Hasegawa, T., Aozasa, S., Matsui, H., and Motoyama, M., *J. Alloys Compds.* **193**, 298 (1993).
6. Ranga Rao, G., Kaspar, J., Di Monte, R., Meriani, S., and Graziani, M., *Catal. Lett.* **24**, 107 (1994).
7. Fornasiero, P., Di Monte, R., Ranga Rao, G., Kaspar, J., Meriani, S., Trovarelli, A., and Graziani, M., *J. Catal.* **151**, 168 (1995).
8. Vlaic, G., Fornasiero, P., Geremia, S., Kaspar, J., and Graziani, M., *J. Catal.* **168**, 386 (1997).
9. Kaspar, J., de Leitenburg, C., Fornasiero, P., Trovarelli, A., and Graziani, M., *J. Catal.* **146**, 136 (1994).
10. Michalowicz, A., “Logiciel pour la Chimie,” p. 751. Societé Francaise de Chimie, Paris, 1991.
11. Lengeler, B., and Eisenberger, P., *Phys. Rev. B* **49**, 11652 (1994).
12. Vlaic, G., Navarra, G., Regnard, J.-R., Williams, C. E., and Jérome, R., *J. Phys. II Fr.* **5**, 665 (1995).
13. McKale, A. G., Veal, B. W., Paulikas, A. P., Shaw, S. K., and Knapp, G. J., *J. Am. Chem. Soc.* **110**, 3763 (1988).
14. Sevillano, E., Meuth, H., and Rehr, J. J., *Phys. Rev. B* **20**, 4908 (1979).
15. Stern, E. A., *in* “X-ray Absorption: Principles, Applications, Techniques of EXAFS, SEXAFS and XANES” (D. C. Koningsberger and R. Prins, Eds.), Chemical Analysis, Vol. 92, p. 37. Wiley–Interscience, New York, 1988.
16. Stern, E. A., *Phys. Rev. B* **48**, 9825 (1993).
17. Michalowicz, A., and Vlaic, G., *J. Synchr. Radiat.* **5**, 1317 (1998).
18. McHale, A. E., “Phase Diagrams for Ceramists: Annual 1991,” p. 20, 1991.
19. Meriani, S., *Mater. Sci. Eng. A Struct. Mater.* **71**, 365 (1985).
20. Yashima, M., Arashi, H., Kakihana, M., and Yoshimura, M., *J. Am. Ceram. Soc.* **77**, 1067 (1994).
21. Yashima, M., Sasaki, S., Kakihana, M., Yamaguchi, Y., Arashi, H., and Yoshimura, M., *Acta Crystallogr. B Struct. Sci.* **50**, 663 (1994).
22. Yashima, M., Hirose, T., Katano, S., Suzuki, Y., Kakihana, M., and Yoshimura, M., *Phys. Rev. B Condens. Matter* **51**, 8018 (1995).
23. Yashima, M., Morimoto, K., Ishizawa, N., and Yoshimura, M., *J. Am. Ceram. Soc.* **76**, 1745 (1993).
24. Meriani, S., *Mater. Sci. Eng. A Struct. Mater.* **109**, 121 (1989).
25. Keramidas, V. G., and White, W. B., *J. Am. Ceram. Soc.* **57**, 22 (1974).
26. Smith, D. K., and Newkirk, H. W., *Acta Crystallogr.* **18**, 983 (1965).
27. Graham, G. W., Weber, W. H., Peters, C. R., and Usmen, R. K., *J. Catal.* **130**, 310 (1991).
28. Hartmanova, M., Poulsen, F. W., Hanic, F., Putyera, K., Tunega, D., Urusovskaya, A. A., and Oreshnikova, T. V., *J. Mater. Sci.* **29**, 2152 (1994).
29. Ranga Rao, G., Fornasiero, P., Di Monte, R., Kaspar, J., Vlaic, G., Balducci, G., Meriani, S., Gubitosa, G., Cremona, A., and Graziani, M., *J. Catal.* **162**, 1 (1996).
30. Wang, Y. R., Lu, K. Q., Wang, D. H., Wu, Z. H., and Fang, Z. Z., *J. Phys. Condens. Matter* **6**, 633 (1994).
31. Li, P., Chen, I. W., and Penner-Hahn, J. E., *J. Am. Ceram. Soc.* **77**, 118 (1994).
32. Li, P., Chen, I. W., and Penner-Hahn, J. E., *J. Am. Ceram. Soc.* **77**, 1289 (1994).
33. Li, P., Chen, I. W., and Penner-Hahn, J. E., *Phys. Rev. B* **48**, 10063 (1993).
34. Li, P., Chen, I. W., and Penner-Hahn, J. E., *J. Am. Cerami. Soc.* **77**, 1281 (1994).
35. Balducci, G., Fornasiero, P., Di Monte, R., Kaspar, J., Meriani, S., and Graziani, M., *Catal. Lett.* **33**, 193 (1995).
36. Vidmar, P., Fornasiero, P., Kaspar, J., and Graziani, M., *J. Catal.* **171**, 160 (1997).